Structure of *Toxoplasma gondii* LDH1: Active-Site Differences from Human Lactate Dehydrogenases and the Structural Basis for Efficient $APAD^+$ Use[†,‡]

Kathryn L. Kavanagh, Robert A. Elling, and David K. Wilson*

Section of Molecular and Cellular Biology, University of California, Davis, California 95616

Received June 27, 2003; Revised Manuscript Received October 21, 2003

ABSTRACT: While within a human host the opportunistic pathogen *Toxoplasma gondii* relies heavily on glycolysis for its energy needs. Lactate dehydrogenase (LDH), the terminal enzyme in anaerobic glycolysis necessary for NAD^+ regeneration, therefore represents an attractive therapeutic target. The tachyzoite stage lactate dehydrogenase (LDH1) from the parasite *T. gondii* has been crystallized in apo form and in ternary complexes containing NAD^+ or the NAD^+-analogue 3-acetylpyridine adenine dinucleotide ($APAD^+$) and sulfate or the inhibitor oxalate. Comparison of the apo and ternary models shows an active-site loop that becomes ordered upon substrate binding. This active-site loop is five residues longer than in most LDHs and necessarily adopts a different conformation. While loop isomerization is fully rate-limiting in prototypical LDHs, kinetic data suggest that LDH1's rate is limited by chemical steps. The importance of charge neutralization in ligand binding is supported by the complexes that have been crystallized as well as fluorescence quenching experiments performed with ligands at low and high pH. A methionine that replaces a serine residue and displaces an ordered water molecule often seen in LDH structures provides a structural explanation for reduced substrate inhibition. Superimposition of LDH1 with human muscle- and heart-specific LDH isoforms reveals differences in residues that line the active site that increase LDH1's hydrophobicity. These differences will aid in designing inhibitors specific for LDH1 that may be useful in treating toxoplasmic encephalitis and other complications that arise in immune-compromised individuals.

Toxoplasma gondii is a protozoan parasite from the phylum *Apicomplexa* that also includes the important human pathogens *Plasmodium* and *Cryptosporidium* (*2*). These organisms have complex life cycles that include both sexual and nonsexual reproduction (*3*−*5*). Sexual reproduction for *T. gondii* takes place exclusively in felines, but the organism has a broad intermediate host range in which nonsexual reproduction occurs. Intermediate hosts become infected by ingesting cysts or oocytes in contaminated food or water. In humans, transplacental infection results in significant fetal morbidity and mortality (*6*). *T. gondii* is also one of the most common opportunistic AIDS pathogens with toxoplasmic encephalitis or pneumonia often causing death (*7*, *8*). In contrast, infection is often asymptomatic in immunocompetent individuals and progresses from a rapidly replicating tachyzoite stage to a dormant bradyzoite stage in response to the immune system, progresses from a rapidly replicating tachyzoite stage to a dormant bradyzoite stage. Bradyzoites remain encapsulated in glucose-rich tissues such as muscle and brain and may cause recrudescent infections.

While within human hosts, apicomplexan organisms derive much of their energy from anaerobic glycolysis. This reliance implies that disruption of glycolysis may be a viable means to develop new treatments. It has been suggested that the terminal enzyme in glycolysis, lactate dehydrogenase (LDH),[1] therefore represents a judicious target for drug therapy against these organisms (*9*). Compounds that inhibit LDH have also been shown to inhibit growth of *Plasmodium falciparum* in cultured erythrocytes (*10*) and *T. gondii* tachyzoites in cultured fibroblasts (*11*). *T. gondii* differentially expresses two forms of LDH with 71% amino acid identity: LDH1 in rapidly growing tachyzoites and LDH2 in more slowly replicating bradyzoites (*11*, *12*). Bradyzoites are encysted, resistant to the immune system and chemotherapy, and are the source of recurrent infections. Both isoforms are targets for the design of therapeutic inhibitors and share a number of strictly conserved residues with other LDHs including Arg109, Arg171, and the catalytic dyad His195/Asp168.

[†] This work was supported by a grant from the National Institutes of Health to D.K.W. and the Keck Foundation. K.L.K. is supported by a grant from the University of California Systemwide Biotechnology Research Program, proposal number 2001-07. The data collection facilities at Stanford Synchrotron Radiation Laboratory are funded by the U.S. Department of Energy and by the National Institutes of Health.

[‡] The coordinates have been deposited into the Protein Data Bank under the following ID codes: 1PZE (LDH1 apoenzyme), 1PZH (LDH1 complex with NAD^+ and oxalate), 1PZF (LDH1 complex with $APAD^+$ and oxalate), and 1PZG (LDH1 complex with $APAD^+$ and sulfate).

* To whom correspondence should be addressed. Phone: (530) 752-1136. Fax: (530) 752-3085. E-mail: dave@alanine.ucdavis.edu.

[1] Abbreviations: $APAD^+$, oxidized 3-acetylpyridine adenine dinucleotide; bsLDH, *Bacillus stearothermophilus* LDH; DHPR, *Escherichia coli* dihydrodipicolinate reductase; hLDH-A_4, homotetrameric human muscle LDH; hLDH-B_4, homotetrameric human heart LDH; LDH1, *Toxoplasma gondii* tachyzoite LDH; LDH2, *T. gondii* bradyzoite LDH; pfLDH, *Plasmodium falciparum* LDH; LDH, lactate dehydrogenase; NAD^+, oxidized nicotinamide adenine dinucleotide; NADH, reduced nicotinamide adenine dinucleotide; OXL, oxalate; OXM, oxamate; rmsd, root-mean-square deviation; SSRL, Stanford Synchrotron Radiation Laboratory.

10.1021/bi035108g CCC: $27.50
Published on Web 01/07/2004

In general, LDHs follow an ordered kinetic mechanism in which addition of NAD^+ precedes binding of lactate. Residues 95−113 comprise a mobile loop, commonly referred to as the substrate-specificity loop. Upon substrate binding, this segment closes over the active site sequestering it from solvent. Hydride transfer to the A side of the nicotinamide and proton abstraction by His195 are facilitated by Arg109 and Asp168, which stabilize the tetrahedral oxyanion transition state and the protonated histidine, respectively. The Arg171 side chain anchors the substrate into position by forming bidentate hydrogen bonds with its carboxylate. Reopening of the loop is followed by sequential release of pyruvate and NADH. The mechanism has been well-characterized for pig muscle LDH for which the rate-limiting step in the lactate to pyruvate direction occurs after hydride transfer and is most likely loop opening since the rates of NADH and pyruvate release are inferred to be fast (*13*−*15*). In the reverse direction, the rate-limiting step is loop closing (i.e., it is the loop isomerization that takes place when pyruvate is in the binding pocket). This analysis is generally believed to be applicable to all known LDHs.

When compared to vertebrate and bacterial LDH's, *T. gondii* LDHs share a number of unique structural and kinetic features with *P. falciparum* LDH (pfLDH) (*11*). These include a substrate-specificity loop that is extended by five amino acids (Figure 3A). In LDH2 and pfLDH, this insert is identical (KSDKE), whereas the insert in LDH1 is slightly different (KPDSE). A serine at position 163 observed to interact with the nicotinamide amide in all nonapicomplexan LDH crystal structures is replaced by a leucine in pfLDH and methionine in LDH1 and LDH2. In the reducing (pyruvate to lactate) direction, most LDHs are inhibited by high concentrations of pyruvate. LDH2 and pfLDH show a complete lack of this substrate inhibition, while LDH1 exhibits reduced substrate inhibition. Despite the fact that specific activity with the NAD^+ analogue 3-acetylpyridine adenine dinucleotide ($APAD^+$) is reduced for most LDHs, it has been found that LDH1, LDH2, and pfLDH all exhibit enhanced catalytic efficiency with this cofactor (*11*, *16*). In fact, this ability to efficiently use $APAD^+$ has been exploited in a diagnostic test for malaria (*17*).

Although a leucine or methionine at position 163 is unusual for lactate dehydrogenases, it is common in the closely related malate dehydrogenases. These two enzyme families share a similar framework and are evolutionarily related most likely by early gene duplication and divergence. A phylogenetic reconstruction reveals that apicomplexan LDHs are most closely related to α-proteobacterial malate dehydrogenases (*18*). The analysis suggests that apicomplexan LDHs have evolved from a malate dehydrogenase of α-proteobacterial origin by lateral gene transfer or endosymbiosis. This is plausible since a single residue change has been used to convert a lactate dehydrogenase into a malate dehydrogenase although the rational conversion from a malate to a lactate dehydrogenase has not yet been demonstrated (*19*). Therefore, the unique features apicomplexan LDHs possess may be a result of their late stage evolution from a malate dehydrogenase.

Structural characterization was pursued to provide an explanation for these unique features that LDH1 possesses. The information provided by the atomic resolution structure is the first step toward structure-based design of new treatments for toxoplasmic infection.

EXPERIMENTAL PROCEDURES

Cloning, Expression, and Purification. A plasmid encoding the *T. gondii* LDH1 gene was a kind gift from Dr. Stephen Parmley (*11*). Wild-type LDH1 was amplified using the primers 5′GCTAGTC**CATATG**GCACCCGCACTTGTGCAGAGG3′ (forward) and 5′ACTG**CCCGGG**CGCCTGAAGAGCAGCAACCGC3′ (reverse) and cloned into pTYB2 (NEB) for expression as an intein chitin-binding domain fusion protein. The *Nde*I and *Sma*I sites used for cloning are shown in bold. The coding region was sequenced to ensure that mutations were not present. Competent *E. coli* BL21* (Invitrogen) were transformed with the plasmid and used for expression. Cells were grown in LB medium containing 100 μg/mL ampicillin to an optical density at 600 nm of 0.6, equilibrated to 15 °C, and induced with 0.5 mM IPTG. After 12 h, cells were harvested by centrifugation and resuspended in column buffer A (20 mM Tris, 0.5 M NaCl, 1 mM EDTA, 0.1% Triton X-100, pH 8.0). All subsequent steps were performed at 4 °C. Cells were disrupted by microfluidization, and debris was removed by centrifugation at 39 000*g* for 30 min. The clarified supernatant was applied to a 15 mL chitin column (NEB) and washed with 20 column volumes of buffer A. The column was then washed with the same buffer without Triton X-100 (buffer B) until the absorbance at 280 nm reached a baseline. Cleavage on the column was initiated by loading with buffer B containing 40 mM β-mercaptoethanol, stopping the flow, and incubating overnight. After elution with buffer B, LDH1 was concentrated and exchanged into 20 mM Tris, pH 7.5 using a Millipore centrifugal filter with a 30 kDa molecular weight cutoff. This concentrate was applied to a 10 mL reactive green 5 (Sigma) column, washed briefly, and eluted in 20 mM Tris, 250 mM NaCl, pH 7.5. The buffer was replaced with 10 mM Tris, 50 μM EDTA, pH 7.5, and the protein was concentrated to 12 mg/mL.

Crystallization. A sparse matrix approach was used to screen conditions for crystal growth. The best apo LDH1 crystal was grown at 293 K by suspending a drop containing 6 mg/mL LDH1, 1 mM gossylic iminolactone (provided by Prof. David Vander Jagt), 12% w/v poly(ethylene glycol) 1000, 50 mM phosphate-citrate, pH 4.2 over a well containing 24% w/v poly(ethylene glycol) 1000, 100 mM phosphate-citrate, pH 4.2. Ternary complex crystals of LDH1 were grown by mixing equal volumes of 12 mg/mL LDH1 containing 10 mM cosubstrate and 5 mM oxalate or oxamate with a well solution consisting of 0.85−0.90 M ammonium sulfate, 100 mM acetate, pH 4.5. In all cases, the crystals were transferred to a cryo-protectant solution consisting of 25% v/v glycerol, 75% v/v well solution before being flash-cooled in a stream of nitrogen gas at 100 K.

Data Collection, Refinement, and Analysis. Data were collected at Stanford Synchrotron Radiation Laboratory (SSRL) beamlines 7-1, 9-1, and 9-2 and were processed and scaled with DENZO and SCALEPACK (*20*). This is summarized in Table 1. A molecular replacement solution for the apo LDH1 structure was found using the program EPMR (*21*) and the pfLDH monomer (PDB accession 1LDG) (*22*) with ligands and waters removed as a search model. Data in

Table 1: Summary of LDH1 Data Collection, Refinement, and Models

	apoLDH1	LDH1−NAD^+−OXL	LDH1−$APAD^+$−SO_4	LDH1−$APAD^+$−OXL
		Data Collection		
	MAR345 SSRL 9-1	MAR345 SSRL 9-1	MAR345 SSRL 7-1	ADSC CCD SSRL 9-2
spacegroup	$I4_122$	$P2_1$	$P2_1$	$P2_1$
unit cell	$a = b = 77.46$ Å $c = 218.58$ Å	$a = 68.07$ Å $b = 125.12$ Å $c = 86.60$ Å $\beta = 106.08$ °	$a = 67.94$ Å $b = 124.98$ Å $c = 86.39$ Å $\beta = 105.96$ °	$a = 68.06$ Å $b = 124.98$ Å $c = 86.69$ Å $\beta = 106.09$ °
resolution (Å)	30−1.95 (1.98−1.95)[a]	30−1.9 (1.93−1.9)	30−1.6 (1.63−1.6)	30−2.2 (2.24−2.2)
observations/unique reflections	141 594/24 776	223 205/103 102	451 492/167 180	224 085/70 313
R_{merge}	0.043 (0.349)	0.071 (0.326)	0.036 (0.346)	0.121 (0.386)
completeness (%)	99.9 (99.8)	94.2 (91.8)	91.8 (92.5)	99.1 (91.7)
$I/\sigma(I)$	35.7 (4.5)	12.6 (3.1)	25.3 (2.6)	9.2 (2.9)
		Refinement		
reflections used ($I > 0$): total/test set	24 745/1236	103 053/5142	167 149/8417	70 134/3559
R_{cryst}	0.1876	0.1644	0.1762	0.1775
R_{free}	0.2220	0.2000	0.1976	0.2176
rmsd bond length (Å)[b]	0.016	0.015	0.010	0.009
rmsd bond angle (°)	1.64	1.63	1.47	1.41
		Final Model		
protein atoms	2438	9880	9865	9872
ligand atoms		200	196	200
water molecules	100	588	562	374
β-mercaptoethanol atoms			16	
Ramachandran most favored	90.0%	93.2%	92.8%	91.6%

[a] Values in parentheses are for data in highest shell. [b] rmsd, root-mean-square deviation.

the range of 20−4 Å resulted in a single solution that gave a correlation coefficient of 0.386 and initial crystallographic *R*-factor of 0.498. Initial phases were calculated for the ternary complex of LDH1 with NAD^+ and oxalate (LDH1−NAD^+−OXL) using molecular replacement implemented by EPMR and the apo LDH1 tetramer as a search model. Data in the range of 15−4 Å resulted in a solution for which the correlation coefficient equaled 0.564 and the initial *R*-factor was 0.420. The LDH1−$APAD^+$ complex unit cell was isomorphous with the LDH1−NAD^+−OXL ternary complex; therefore, the LDH1−NAD^+−OXL ternary complex was used as a starting model. In each case, before refinement commenced, 5% of the data was flagged for the calculation of a free *R*-factor. The final structures were obtained by alternating rounds of refinement in CNS (*23*) and manual fitting in O (*24*) with waters picked in CNS and manually checked for proper hydrogen bonding and electron density. The program LSQKAB was used for structural superimpositions and determination of root-mean-square deviations (*25*).

Studies of Ligand Binding Using Change in Protein Fluorescence. The decrease in protein fluorescence upon forming a ternary complex was used to calculate ligand dissociation constants from the LDH1−NAD^+ complex. Fluorescence measurements were recorded at 25 °C on an AMINCO−Bowman series 2 luminescence spectrometer equipped with a thermostated cell. Emission at 340 nm was monitored after excitation at 290 nm. Protein solutions contained 5 μM LDH1 and 100-fold molar excess NAD^+ in either 50 mM Bis-Tris, pH 6.0 or 50 mM Tris, pH 9.2. Ligand concentrations typically ranged from 0 to 5 mM. Stock solutions of sodium sulfate and sodium oxamate were titrated to the pH of the assay. Data were fit to a hyperbolic binding curve using KaleidaGraph version 3.09.

Steady-State Enzyme Kinetics. LDH1 activity for the reduction of pyruvate to lactate was measured at 25 °C in 100 mM Tris, pH 7.5. Data were collected on a Hewlett-Packard 8453 UV−vis spectrophotometer equipped with a temperature-controlled cell holder. Enzyme concentration was 7.2 nM, cofactor concentration was constant and saturating at 180 μM, and pyruvate concentration varied from 0 to 40 mM. The assay volume was 1 mL, and reactions were initiated by the addition of pyruvate ($\leq$50 μL). Initial rates of decrease in NADH were followed at 340 nm with $\epsilon = 6220\ M^{-1}\ cm^{-1}$. The decrease in APADH concentration was monitored at 363 nm using a molar extinction coefficient of $9100\ M^{-1}\ cm^{-1}$ (*26*). Appropriate corrections were made for background rates. Nonlinear regression using KaleidaGraph version 3.09 was employed to fit data to the Michaelis−Menten equation corrected for substrate inhibition: $v/v_{max} = S/[K_m + S + (S^2/K_i)]$.

RESULTS AND DISCUSSION

The model for apo LDH1 includes residues 14-103C and 105B-332 of a single monomer.[2] Two residues at the N-terminus, the Lys-Pro-Asp of the inserted KPDSE motif on the active-site loop, and one residue at the C-terminus were disordered and not fit. The tetramer is constructed crystallographically by two folds present in the $I4_122$ symmetry. The final model also includes 100 water molecules.

[2] To preserve active-site nomenclature, LDHs are commonly numbered according to the initial assignment of residues from the X-ray structure of dogfish muscle LDH (*1*). Since the primary sequence was not available at that time, errors were made that consequently required the elimination of some numbers and the insertion of others. Insertions relative to this reference have a letter appended to the residue number (i.e., 103B). LDH1 consists of 329 residues that are numbered from the initiator methionine at residue 12 to the C-terminal residue, Ala333. Insertions occur at seven places in the sequence wherein amino acid designations have a letter appended to the number.

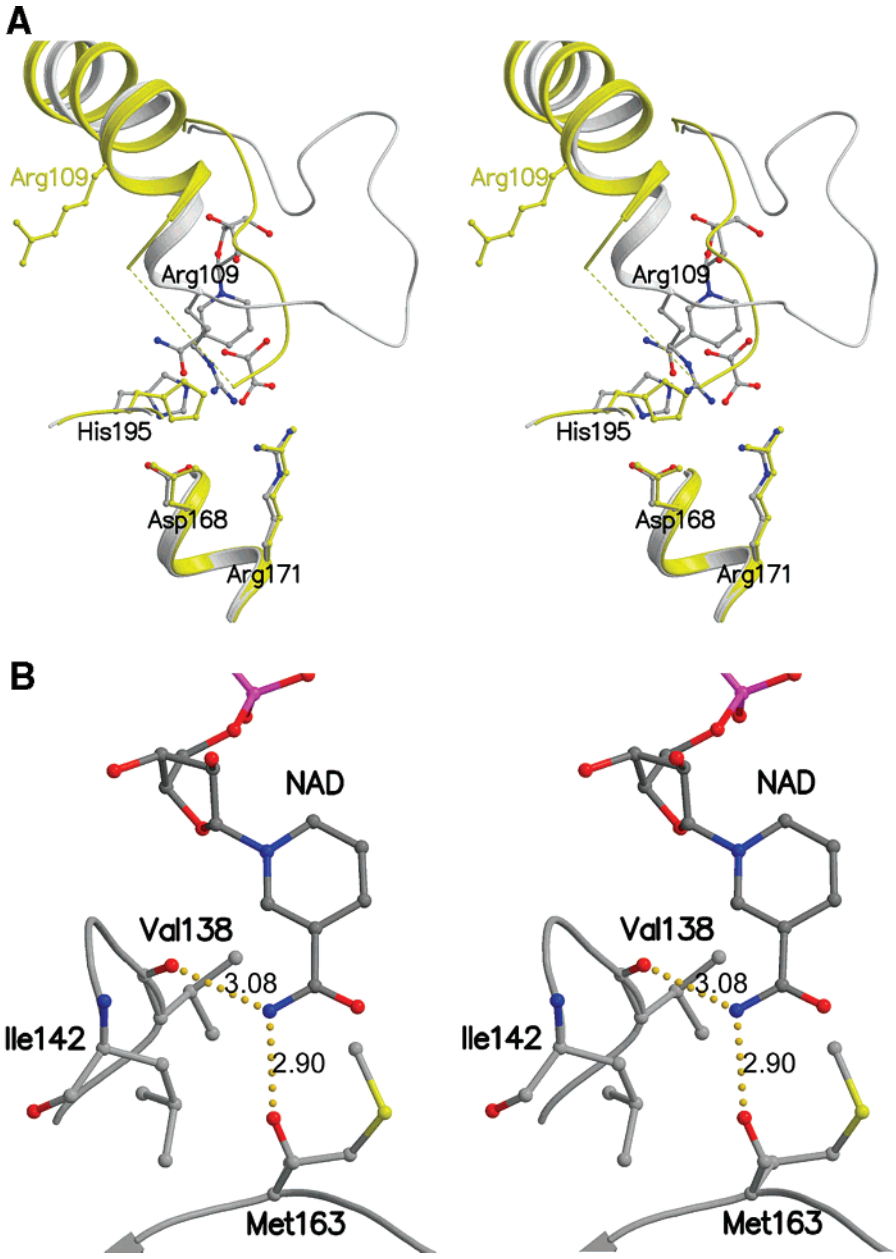

FIGURE 1: LDH1−NAD^+−OXL monomer A is drawn colored by atom type with carbon gray, oxygen red, nitrogen blue, sulfur yellow, and phosphorus pink. (A) Apo LDH1 in yellow is superimposed upon LDH1−NAD^+−OXL. Three disordered residues in the apo structure are represented by a dashed line. A substrate-induced loop isomerization brings Arg109 into the active site. The conserved His195/Asp168 catalytic dyad, Arg109, Arg171, NAD^+, and oxalate are drawn in ball-and-stick. (B) Hydrogen bonds between the protein and the NAD^+ amide are portrayed as dotted yellow lines with distances given in angstroms. Figures 1, 2A, and 3B were created using MolScript (*37*) and Raster3D (*38*).

The asymmetric units for the ternary complexes encompass a full tetramer. The ternary model of LDH1 with NAD^+ and oxalate (LDH1−NAD^+−OXL) contains residues 14−335 of monomers A and B and residues 14−332 of monomers C and D. There are also one NAD^+ and one oxalate per subunit and 588 water molecules. The cloning procedure resulted in an extra Pro-Gly at the C-terminus corresponding to residues 334 and 335. The ternary model of LDH1 with $APAD^+$ and sulfate (LDH1−$APAD^+$−SO_4) includes residues 14−334 of monomers A and B, residues 15−332 of monomer C, and residues 14−332 of monomer D. Also found were one $APAD^+$, one sulfate ion, and one covalently attached molecule of β-mercaptoethanol per subunit and 562 water molecules. The ternary model of LDH1 with $APAD^+$ and oxalate (LDH1−$APAD^+$−OXL) includes residues 14−334 of monomers A and B, residues 14−332 of monomers C and D, one $APAD^+$ and one oxalate per subunit, and 374 water molecules. All residues were in allowed regions of a Ramachandran plot as calculated by PROCHECK (*27*). Refinement results are summarized in Table 1.

Substrate-Induced Loop Closure. Overall, the models are largely similar with the highest root-mean-square deviation (rmsd) between the apo model and any of the ternary complexes. Three residues on the substrate specificity loop, Lys-Pro-Asp of the five amino acid insert, become ordered upon substrate binding (Figure 1A). Residues at the N-terminus of helix α4 (107−114) move approximately 7 Å, and the Cα of Arg-109 moves 10 Å as it is recruited into the active site to hydrogen bond with substrate (Figure 1). The main chain of residue 107 makes a crystal contact in

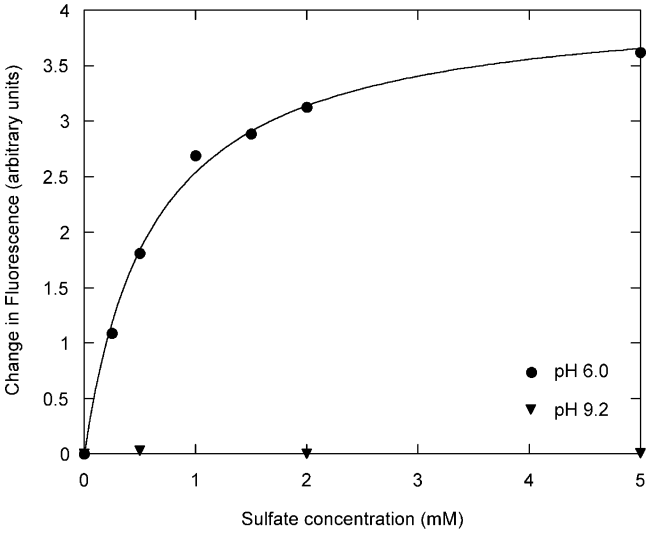

FIGURE 2: Titration curve for binding of sulfate to the LDH1−NAD^+ complex. The fit of data obtained at pH 6.0 to a hyperbolic curve is represented by a line.

the apo structure that may stabilize an extra turn of helix α4. This region is not involved in crystal packing in the ternary complexes. The rmsd for all α carbons between apo model and monomer A from the LDH1−NAD^+−OXL ternary complex is 2.0 Å. The extended loop region containing residues 88−105 exhibits the largest differences. When residues 88−105 are removed from the calculation, the rmsd for α carbons is 0.5 Å. The rmsd for α carbons between monomer A from the LDH1−NAD^+−OXL complex and all other ternary complex monomers varies from 0.2 to 0.4 Å, demonstrating that all the ternary complexes are highly homologous.

Charge Balance and Extended Loops in the Active Site. The fact that oxamate was included in one of the crystallization conditions but sulfate was incorporated into the crystals instead lends credence to the hypothesis that charge balance is important in the active site (*19*, *28*). This has been used as a paradigm for how lactate and malate dehydrogenases discriminate between their substrates. In this model, for LDHs, the net charge of substrates plus the charge on His195 must sum to zero. This can be accomplished during the catalytic cycle by His(+1), pyruvate(−1), and NADH-(0) or His(0), lactate (−1), and NAD^+(+1).

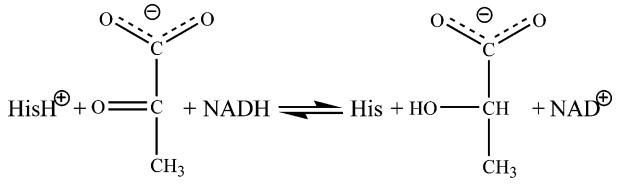

Pyruvate L-Lactate

Since malate carries an additional negative charge, an additional positively charged arginine is usually found on the active-site loop in malate dehydrogenases. In fact, mutating Gln102 to arginine changes *Bacillus stearothermophilus* LDH (bsLDH) to a specific and efficient malate dehydrogenase (*19*). As the LDH1 crystals were grown in the presence of NAD^+ at pH 4.2−4.5 where His195 would most likely be protonated, a charge of −2 on the second ligand is needed to balance the two positive charges. Thus, sulfate (−2) or oxalate (−2) fulfills the charge requirement, while oxamate (−1) does not.

To further investigate ligand binding to the LDH1−NAD^+ complex, we tried to assay lactate oxidation at low pH (6.0−7.5). Unfortunately, the reaction proceeds slowly at this pH even in the absence of inhibitors and would have required extraordinarily high enzyme concentrations. As LDH1 has only one tryptophan that is shown in the crystal structures to be solvent exposed in the apoenzyme and sequestered in ternary complexes, we studied ligand binding by observing changes in protein fluorescence. Sulfate binds to the LDH1−NAD^+ complex at pH 6.0 with a dissociation constant of 0.62 (±0.05) mM (Figure 2). The binding is dependent on NAD^+ with no change in fluorescence if NAD^+ is not included in the conditions. Conversely, at pH 9.2, concentrations of sulfate up to 200 mM were tested, and there was no detectable binding to the LDH1−NAD^+ complex. Dissociation constants for oxamate to LDH1−NAD^+ were calculated to be 1.11 (±0.07) mM at pH 6.0 and 3.14 (0.27) mM at pH 9.2. These results were unanticipated given that the charge neutralization theory predicted that oxamate would bind better at high pH. From previous crystal structures, oxamate is expected to bind with the carbonyl oxygen adjacent to His195; however, a productive hydrogen bond will form only if the histidine is protonated. Evidently, this hydrogen bond facilitates ligand binding. Although we did not look at binding to the LDH1−NADH complex, we expect oxamate to bind tightest to the LDH1−NADH complex at low pH where both hydrogen bonding with His195 is optimized and charges sum to zero. Admittedly, the sulfate concentration was high relative to oxamate (0.9 M vs 5 mM), but identical conditions using oxalate yielded oxalate in the crystals. So while charge balance may be an important component of binding, clearly it is not the only determinant, and other factors such as optimized hydrogen bonding and van der Waals interactions are conceivably just as significant. This charge balance in the active site could be important in inhibitor design as discussed below.

LDH1 has inserts in two loop regions that seal the active site from solvent in the closed conformation (Figure 3A). The elongated substrate-specificity loop has also been observed in pfLDH, and the conformation of this loop is similar (*22*). The two amino acid insert on the opposing side of the cleft, Leu-Gly at position 242, is however novel. The Nζ of Lys102 hydrogen bonds with the carbonyl oxygen of Gly242C over the active-site cleft stabilizing the closed conformation. Although this is the only polar interaction between these two loops, there are van der Waals contacts between the Trp107 side chain on the substrate-specificity loop and Gly237 and the side chain of Val240 on the opposing loop.

Active-Site Differences in LDH1 versus Human LDHs. Since the *T. gondii* parasite relies heavily on glycolysis for its energy requirements, inhibitors specific for LDH1 over human LDHs would be of value in designing new treatments for toxoplasmosis. LDH1 shares 30 and 29% amino acid identity, respectively, with human muscle (hLDH-A_4) and human heart (hLDH-B_4) isoforms of LDH. To investigate the differences between human and parasitic enzymes, we superimposed LDH1 with the NADH- and oxamate-bound hLDH-A_4 (PDB accession 1I10) and hLDH-B_4 (PDB accession 1I0Z) structures (*29*). This reveals a number of

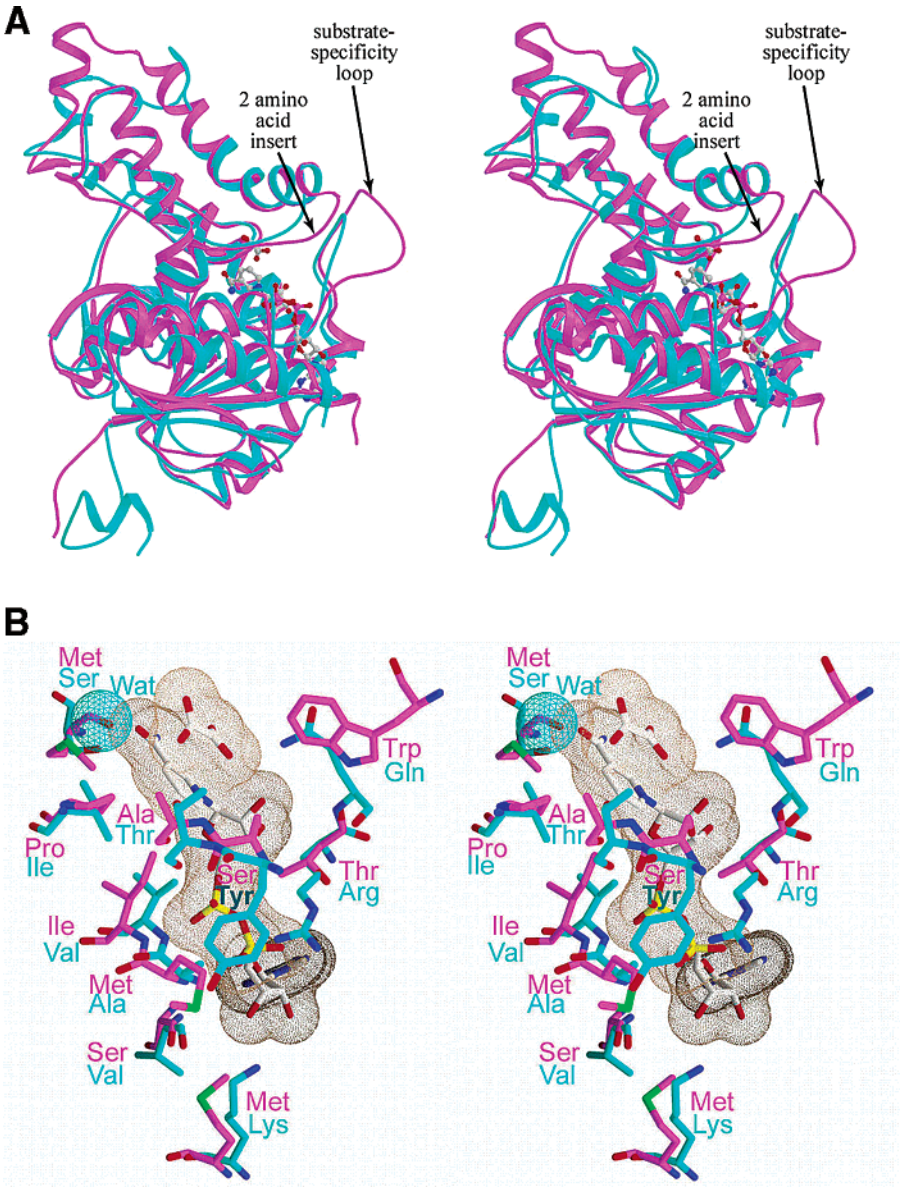

FIGURE 3: Superimposition of LDH1−NAD^+−OXL monomer A (purple) with hLDH-A_4−NADH−OXM monomer A (cyan). (A) α-Carbon traces illustrating the longer active-site loops in LDH1. NAD^+ and oxalate from the LDH1 ternary complex are drawn in ball-and-stick representation. The different conformation of the substrate-specificity loop due to the five amino acid insert is evident, and the two amino acid insert at residue 242 is on the opposing side of the cleft. (B) Close-up of the active site. Ligands from the LDH1−NAD^+−OXL complex are depicted in ball-and-stick with their molecular surface represented in gold. The conserved water observed in the hLDH-A_4 complex is portrayed as a space-filling mesh sphere. The program GRASP (*39*) was used to make Figure 2B.

Table 2: Active-Site Differences between LDH1 and Human LDH Isoforms

residue	LDH1	hLDH-A_4	hLDH-B_4
28	Ser	Val	Val
30	Met	Ala	Gln
31	Ile	Val	Val
58	Met	Lys	Lys
101	Thr	Arg	Arg
107	Trp	Gln	Gln
163	Met	Ser	Ser
245	Ser	Tyr	Tyr
246	Ala	Thr	Thr
250	Pro	Ile	Ile

dissimilar residues lining the active-site cavity that are summarized in Figure 3B and Table 2. As hLDH-A_4 and hLDH-B_4 are identical at all these positions except for residue 30, we have used hLDH-A_4 as a model for both. With the exception of Trp107, which occupies the same steric volume as Gln102, these residues are at equivalent positions in the sequences. The overall effect of the substitutions is to increase the hydrophobicity of the LDH1 active site. The main differences are addressed below.

In hLDH-A_4, Arg101 crosses over the cofactor pyrophosphate making a salt link with a phosphate oxygen and stacking with Tyr245. These favorable interactions are expected to stabilize the closed conformation for hLDH-A_4. The equivalent residues in LDH1 are Thr101 and Ser245, which do not contact each other or have polar interactions with the pyrophosphate. In addition, the main chain surrounding Ser245 adopts a different conformation pointing Ser245 into the active site instead of away as seen in Tyr245. In LDH1, Ala246 replaces a threonine in the human isoforms and removes the hydrogen-bond interaction observed between Thr246 and the oxamate carboxylate. Trp107 on the

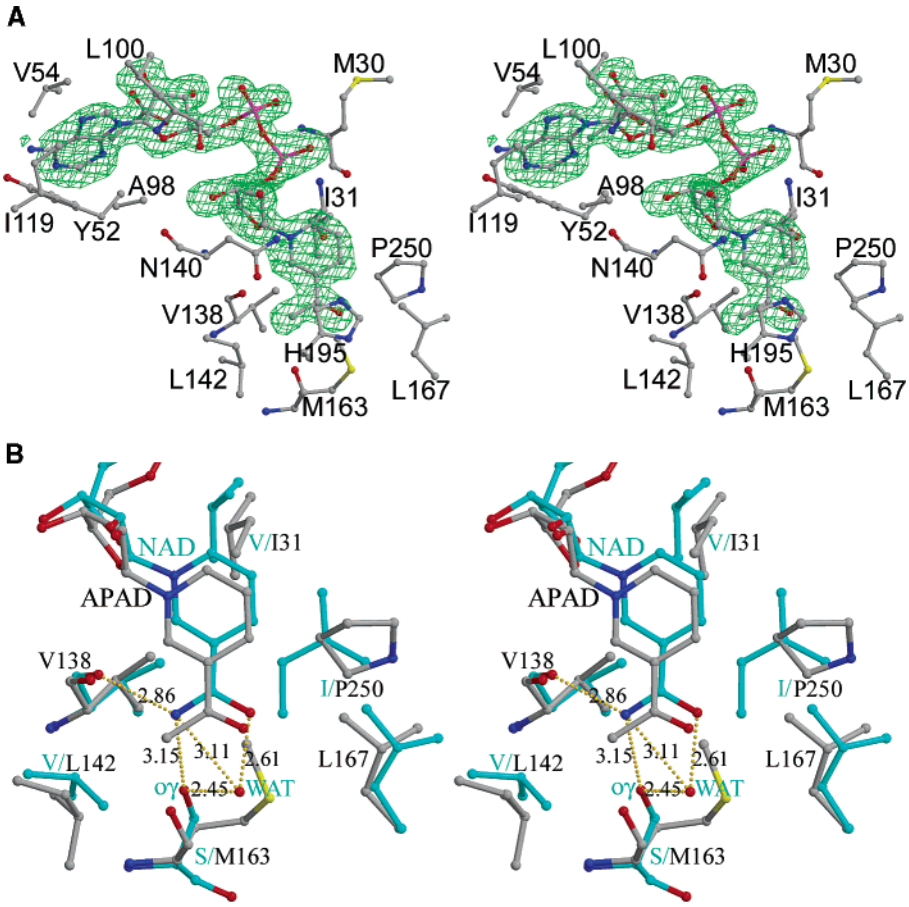

FIGURE 4: APAD$^+$ binding to LDH1 and comparison with NADH-bound hLDH-A$_4$. (A) An $F_o - F_c$ electron density map contoured at 3σ is superimposed upon the final model of LDH1−APAD$^+$−SO$_4$ monomer A. Phases were calculated using the refined model with the APAD$^+$ atoms removed. BobScript (*40*) and Raster3D (*38*) were used to produce Figure 3A. (B) Overlay of LDH1−APAD$^+$−OXL monomer A with hLDH-A$_4$−NADH−OXM monomer A. The LDH1 complex is colored as in Figure 1, and the hLDH-A$_4$ complex is colored cyan. Potential hydrogen bonds in the hLDH-A$_4$ complex involving the amide, water, and serine 163 are shown as dotted yellow lines with distances given in angstroms. Residues are labeled according to LDH1 in black and where hLDH-A$_4$ differs in cyan.

substrate-specificity loop occupies the space that Gln102 occupies in hLDH-A$_4$. Gln102 is highly conserved and interacts with the oxamate nitrogen in ternary complex crystal structures (*29*). Trp107 is obviously unable to make this polar interaction, and its presence enhances the active-site hydrophobicity of LDH1. Ile250, which provides a surface for the pyridine ring to pack against in hLDH-A$_4$, is replaced by a proline, and Ile31 in LDH1 projects further into the NADH-binding pocket than the equivalent valine in human forms. Both of these substitutions are also seen in pfLDH and would be expected to destabilize NADH binding by providing a less favorable surface for the NADH to nestle against. Met163 replaces a highly conserved serine as well as displacing a conserved water molecule found bridging this serine and the nicotinamide. The consequences of this serine to methionine substitution will be discussed in greater detail below. Collectively, this identifies a variety of active-site differences between LDH1 and human LDH isoforms that may be exploited for selective inhibitor design. Combining information about the active-site residues and the appropriate charge on an inhibitor may lead to the design of more potent and selective inhibitors.

Decreased Substrate Inhibition. A common characteristic of LDHs is their susceptibility to substrate inhibition by pyruvate. The accepted mechanism for this inhibition is the enol form of pyruvate binding to the LDH−NAD$^+$ binary complex before NAD$^+$ is released, forming a covalent adduct between NAD$^+$ and pyruvate, which is tightly bound by the enzyme (*30*). Therefore, slow release of NAD$^+$ is thought to be a critical factor. The first LDH that did not exhibit substrate inhibition was pfLDH, and it was predicted to have a leucine at position 163. Subsequent mutation of Ser163 to leucine for hLDH-A$_4$, hLDH-B$_4$, and bsLDH abolished substrate inhibition (*31*−*33*). Surprisingly, while dissociation constants for NADH increase 10−20-fold, the effect is due mainly to decreased affinity for pyruvate as demonstrated by the 50−200-fold increase in pyruvate K_m. This was unexpected since Ser163 is in the NADH-binding pocket and does not make direct contact with pyruvate.

LDH1 and LDH2 both have a methionine at position 163, and LDH2 does not exhibit substrate inhibition. Analysis of Met163 in the LDH1 structures shows that the main chain has adopted a ψ angle of 120° rather than the ~25° observed for serine at this position. This places the carbonyl oxygen of Met163 in position to hydrogen bond with the nicotinamide amide nitrogen (Figure 1B). The methionine side chain precludes binding of a water molecule that usually bridges Oγ of Ser163, the carbonyl oxygen of Gly164, and the NADH amide oxygen. This water likely adds to binding affinity for the cofactor and slows its dissociation increasing susceptibility to substrate inhibition. The amide oxygen makes no polar interactions in LDH1 since the water is

displaced and Michaelis constants for NAD^+ are increased by factors of 4−10 as compared to human LDHs. A similar main-chain conformation and water displacement is observed for Leu163 in pfLDH. Evidence that the water is important is provided by mutants of hLDH-A_4. In studies performed by Holbrook and co-workers, hLDH-A_4 Ser163Leu in which the water is probably displaced is resistant to substrate inhibition, while hLDH-A_4 Ser163Ala in which the water is most likely present is still subject to substrate inhibition (*30*, *33*). Determinants for substrate inhibition must involve more than this single residue, however, since inhibition in LDH1 is reduced when compared to hLDH-A_4 but not eliminated (*11*).

$APAD^+$ Binding and Catalytic Efficiency. Because pfLDH has higher specific activity with $APAD^+$ as compared to NAD^+ and human LDHs have reduced specific activity, increased oxidation of lactate with $APAD^+$ may be used to detect malarial infection (*17*). *T. gondii* LDHs also exhibit increased catalytic efficiency with $APAD^+$ versus NAD^+. While the differential activity with $APAD^+$ may be used to diagnose infection, it is also important to understanding mechanistic differences between parasitic and human LDHs.

The largest conformational change occurs between the unliganded and the ternary complexes, while the NAD^+- and $APAD^+$-bound forms are essentially identical with no side-chain conformational differences in the active site between the three ternary complexes. The conformation of the cofactor in the LDH1−$APAD^+$−OXL and LDH1−$APAD^+$−SO_4 complexes is indistinguishable. The $APAD^+$ methyl group makes eight contacts ≤4 Å with the protein (Figure 4 and Table 3). In both the NAD^+- and the $APAD^+$-bound complexes, the side chain of Ile142 adopts a strained conformation where $\chi 2$ is −80°. Val142 in hLDH-A_4 and hLDH-B_4 occupies similar steric space as the eclipsed Ile142. When the $APAD^+$ complex is compared to the NAD^+-bound form of LDH1, there is a small approximately 7° torsional rotation of the pyridine ring around the glycosidic bond connecting pyridine N1 and ribose C1. This effectively moves the methyl group away from the carbonyl oxygens of Val138 and Met163 to distances of 3.35 and 3.10 Å, respectively. These distances are slightly longer than the 3.08 and 2.90 Å observed in the NAD^+-bound form, but we note that the geometry is consistent with hydrogen-bond distances and angles. While there is increasing evidence for hydrogen bonds involving aromatic carbons as donors in protein−ligand complexes, hydrogen bonds involving aliphatic carbons as donors are not as well-substantiated (*34*). The energy associated with these CH−O interactions may be higher than a standard van der Waals contact, but it is predicted to be lower than a classical hydrogen bond (*35*).

Blanchard and co-workers examined binding of NADH and APADH to *E. coli* dihydrodipicolinate reductase (DHPR) using both X-ray crystallography and microcalorimetry (*36*). In the NADH-bound structure of DHPR, the nicotinamide NH_2 is hydrogen bonded to the carbonyls of Gly102 and Ala126. Replacement of the NADH amine with the methyl group in APADH causes the acetyl group to twist 10° out of coplanarity with the pyridine ring and the methyl group to have van der Waals contacts with two phenylalanines. The distance from the methyl group to the carbonyls of Gly102 and Ala126 is increased to 3.52 and 3.28 Å, respectively, from the distances to the amine of 3.10 and 3.25 Å observed in the NADH-bound structure. These interactions must compensate for the loss of hydrogen bonds as the change in enthalpy for the formation of the two DHPR complexes is similar. An unusual positive change in entropy is associated with the binding of APADH to DHPR, which they suggest may be due to increased conformational flexibility of the main-chain atoms of Ala126 and Ala127. They support this hypothesis by comparing the temperature factors for the main-chain atoms of Ala126−Ala127, which are higher in the APADH-bound structure than in the NADH-bound structure. The increase in entropy upon APADH binding could also be due to desolvation of the methyl group

Table 3: $APAD^+$ Interactions with LDH1

APAD atom	residue (number of interactions; VDW plus hydrogen bonds)[a]
AN1	Val54 (1)
AC2	Tyr52 (1); Val54 (2); Ala98 (1)
AN3	Asp53 (3); Val54 (1); Ala98 (1)
AC4	Val54 (1); Ala98 (1)
AC5	Val54 (2)
AC6	Val54 (1); Ile119 (1)
AN6	Val54 (1); Ile119 (2)
AN7	Val54 (1); Ile119 (1)
AC8	Gly99 (1)
AN9	Asp53 (1); Val54 (1); Gly99 (1)
AC1*	Asp53 (1)
AC2*	Asp53 (2)
AO2*	Asp53 (3);[b] Val54 (1); Val55 (1)
AC3*	Asp53 (2); Wat551 (1)
AO3*	Gly29 (2); Asp53 (3); Met58 (1); Wat551 (1)
AC4*	Asp53 (1)
AO4*	Asp53 (1); Ala98 (2); Gly99 (2)
AC5*	Thr97 (1); Gly99 (1); Wat4 (1)
AO5*	Gly29 (2); Wat4 (1)
AP	Met30 (1); Wat275 (1); Wat363 (1)
AO1	Gly29 (2); Met30 (4); Wat187 (1); Wat275 (1); Wat363 (1)
AO2	Thr101 (1); Wat275 (1)
O3	Thr101 (1); Wat187 (1); Wat275 (1)
NP	Ile31 (2); Thr101 (1); Wat17 (1); Wat187 (1)
NO1	Met30 (1); Ile31 (1); Thr101 (1); Wat17 (1); Wat187 (1)
NO2	Gly29 (1); Met30 (3); Ile31 (4); Wat4 (1)
NC1*	Val138 (1); Asn140 (2)
NC2*	Thr101 (1); Asn140 (1); Wat323 (1)
NO2*	Leu100 (2); Thr101 (1); Leu112 (1); Asn140 (3); Wat323 (1)
NC3*	Leu100 (1); Thr101 (1)
NO3*	Leu100 (2); Asn116 (1); Thr139 (3); Asn140 (1)
NC4*	Thr97 (1)
NO4*	Ile31 (1); Val138 (3); Thr139 (1)
NC5*	Thr97 (3)
NO5*	Ile31 (1); Thr101 (1); Wat17 (1)
NN1	Val138 (2); Asn140 (1)
NC2	Val138 (2); Asn140 (2)
NC3	Val138 (1); Asn140 (1)
NC4	Leu167 (1); Pro250 (2)
NC5	Ile31 (1); Ala246 (1); Pro250 (2); Wat17 (1)
NC6	Ile31 (1); Wat17 (1); Wat323 (1)
NC7	Met163 (2); His195 (2)
NO7	Met163 (2); Ala164 (1); Leu167 (1); His195 (3)
NC8[c]	Val138 (1); Asn140 (1); Leu142 (2); Met163 (1); Ala164 (1); His195 (2)

[a] VDW, van der Waals interactions, are defined as contacts ≤4 Å between any residue atom and $APAD^+$. [b] Underlined residues have one hydrogen-bond interaction ≤ 3.2 Å included in the total. [c] Standard atom designations for NADH are used with the exception of APADH atom NC8 replacing NADH atom NN7.

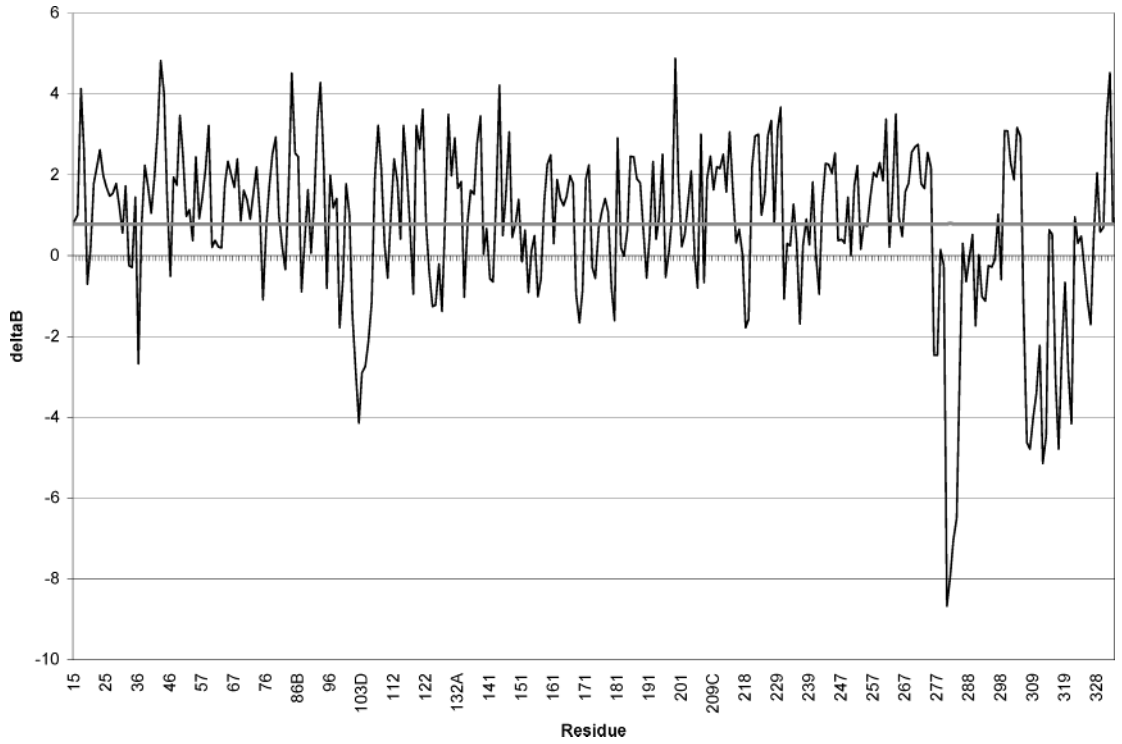

FIGURE 5: Difference in main-chain temperature factor (deltaB; Å^2) is plotted as a function of residue number. A positive value for a residue indicates that the residue has a higher refined *B*-factor in the LDH1−APAD$^+$−OXL complex than in the LDH1−NAD$^+$−OXL complex. The horizontal line indicates the average main-chain *B*-factor difference of 0.78 Å^2.

upon complex formation. We are unaware of other structures besides DHPR of APADH-bound enzymes.

To investigate if higher entropy might play a part in APAD$^+$ binding to LDH1, we compared temperature factors of main-chain atoms in the LDH1−NAD$^+$−OXL and LDH1−APAD$^+$−OXL structures. These structures have comparable average main-chain temperature factors of 14.12 and 14.90 Å^2, respectively. The difference in the average main-chain temperature factor (ΔB; $B_{LDH1-APAD-OXL} - B_{LDH1-NAD-OXL}$) is plotted as a function of residue in Figure 5. A positive value indicates that the APAD$^+$-bound structure has a higher refined *B*-factor. The *B*-factor difference is typically less than 5 Å^2 with the substrate-specificity loop and residues near the C-terminus exhibiting the largest deviations. The C-terminal residues are located on a solvent-accessible loop and helix removed from the active site. Temperature factors for the main-chain atoms of residues that bind the NAD$^+$ amide, Val138 and Met163, are not significantly different. Similar results were obtained when comparing the LDH1−NAD$^+$−OXL and LDH1−APAD$^+$−SO_4 structures, although in that case the residues of the substrate-specificity loop have higher *B*-factors in the APAD$^+$-bound structure (data not shown). This analysis does not support higher entropy for main-chain atoms as a significant contributing factor of APAD$^+$ binding to LDH1.

Comparison of LDH1 structures with ternary complexes of hLDH-A_4 and hLDH-B_4 highlights the presence a conserved water molecule in the human enzyme structures (see *Substrate Inhibition* and Figure 4B). Ser163Leu mutants of hLDH-A_4, hLDH-B_4, and bsLDH are able to use APAD$^+$ more efficiently than wild type (*31*, *32*). For bsLDH, the switch in preference from NAD$^+$ to APAD$^+$ is 3 orders of magnitude due mainly to the mutant's reduced activity with NAD$^+$. For LDH1, increased catalytic efficiency with APAD$^+$ is due to both a ~30-fold increase in k_{cat} and a ~7-fold decrease in K_m for cofactor (*11*). The reduced catalytic efficiency with APAD$^+$ as compared to NAD$^+$ for wild-type hLDH-A_4 and hLDH-B_4 is primarily due to a 20-fold decrease in k_{cat} (*16*). Kinetic constants for LDH1, hLDH-A_4, and hLDH-B_4 with both cofactors are given in Table 4.

Table 4: Kinetic Parameters of LDH1, hLDH-A_4, and hLDH-B_4

steady-state kinetic constant	cofactor used to determine	LDH1	hLDH-A_4	hLDH-B_4
$k_{cat,ox}$ (s^{-1})	NAD$^+$	22[a]	82[b]	50[b]
	APAD$^+$	570[a]	4[b]	2.8[b]
$k_{cat,red}$ (s^{-1})	NADH	64 (2)[e]	300[b]	220[b]
	APADH	30 (2)[e]		
$K_{m,cofactor}$ (μM)	NAD$^+$	348[a]	93[b]	37[b]
	APAD$^+$	50[a]	56[b]	37[b]
	NADH	4.2[a]	5[b]	8[b]
$K_{m,pyruvate}$ (μM)	NADH	359 (34)[e]	170[b]	55[b]
	APADH	814 (147)[e]		
$K_{i,pyruvate}$ (mM)	NADH	31 (3)[e]	0.77[d]	3.9[c]
	APADH	25 (5)[e]	-	-

[a] From ref *11*. [b] From ref *16*. [c] From ref *31*. [d] From ref *30*. [e] Present work, standard errors are indicated in parentheses.

The rate-limiting step in LDH catalysis is generally accepted to be the conformational change accompanying loop opening for the lactate to pyruvate direction, but the five amino acid insert is likely to change loop dynamics in the apicomplexan enzymes. If loop isomerization is rate limiting for LDH1, the increase in k_{cat} implies that the conformational change is faster using APAD$^+$ as compared to NAD$^+$. This could be a result of a less stable ternary complex. The best support for this theory is that Ser163Leu mutants of hLDH-A_4, hLDH-B_4, and bsLDH that have increased activity with APAD$^+$ exhibit a 40−200-fold increase in K_m for pyruvate as compared to wild type. Another possibility is that the conformational change is not fully rate limiting in LDH1.

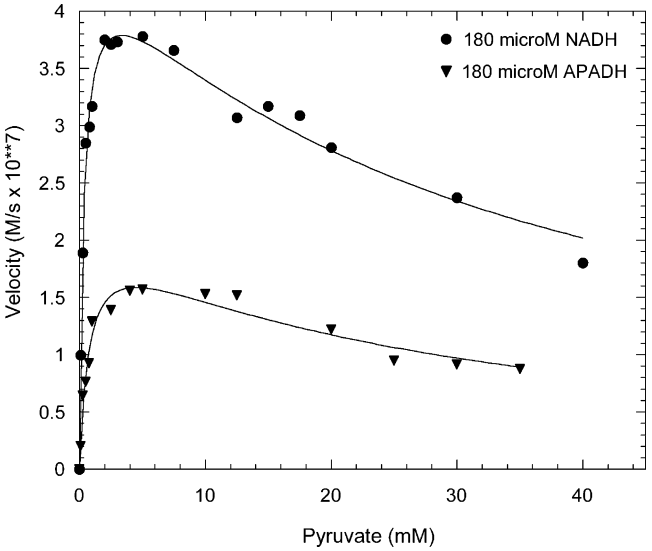

FIGURE 6: Cofactor-dependent LDH1 activity. Initial velocities were measured as a function of pyruvate concentration. NADH and APADH concentrations were constant and saturating at 180 μM. Lines show fit of data to the Michaelis−Menten equation corrected for substrate inhibition (see text for details).

Support for rate limitation by steps other than conformation change is provided by studies of bsLDH. While wild-type bsLDH lacks a significant primary isotope effect on k_{cat} (= 1.1), bsLDH Ser163Leu has a primary kinetic isotope effect of 1.9 indicating that chemical steps have become rate limiting (*31*). Since $APAD^+$ has a higher oxidation potential than NAD^+ (−258 and −320 mV, respectively) hydride transfer to $APAD^+$ occurs faster. Therefore, the increased catalytic efficiency that LDH1 exhibits with $APAD^+$ has two possible origins: either loop opening is rate limiting and occurs faster with $APAD^+$ because the closed conformation is destabilized, or hydride transfer is rate limiting and occurs faster with $APAD^+$ because of its higher oxidation potential.

To investigate the origins of differential cofactor use further, we performed steady-state enzyme kinetics in the pyruvate to lactate direction using both NADH and APADH. Data are presented in Figure 6 and summarized in Table 4. Catalytic rates with NADH were twice that with APADH, while K_m for pyruvate using APADH is 2-fold higher than K_m for pyruvate using NADH. Consider the K_m data first: the higher K_m for pyruvate using APADH suggests that the ternary complex is destabilized relative to the LDH1−NADH−pyruvate complex. This could be the basis for faster loop opening in the lactate to pyruvate direction leading to higher rates for the $APAD^+$ catalyzed reaction. But the catalytic rate data may be more significant. The LDH1-catalyzed reaction proceeds faster with $APAD^+$ versus NAD^+ in the oxidative direction but faster with NADH than APADH in the reductive direction. Because of the differences in oxidation potentials, this is what one would expect if chemical steps were at least partly rate limiting. While this implies LDH1's rate is limited by steps other than conformational change, a more thorough kinetic analysis is required to provide conclusive evidence.

Summary. The LDH1 crystal structures presented here demonstrate the conformational change that takes place upon substrate binding. The substrate-specificity loop in LDH1 is altered both in length and in tertiary structure as compared to vertebrate and bacterial LDHs. Comparison of kinetic parameters determined with NAD(H) and APAD(H) suggests that the conformational isomerization of this loop that is rate limiting in pig muscle LDH is not fully rate limiting in LDH1. Rate-limitation by chemical steps is the apparent origin of LDH1's increased activity with $APAD^+$. Residues lining the active site cavity that differ between LDH1 and human isoforms have been delineated and provide a framework for the design of inhibitors that are selective for *T. gondii* LDH over human LDHs. These amino acid substitutions increase the hydrophobicity of the LDH1 active site relative to human LDHs. Binding experiments as well as the complexes that have been crystallized support the theory that charge balance in the active site is important. This implies that tight-binding active-site inhibitors for the pyruvate to lactate reaction should have a net charge of minus one. A methionine that replaces a more common serine displaces a conserved water molecule and is likely responsible for reduced substrate inhibition.

ACKNOWLEDGMENT

We are grateful to Prof. David Vander Jagt for encouragement and helpful suggestions.

REFERENCES

1. Taylor, S. S., Oxley, S. S., Allison, W. S., and Kaplan, N. O. (1973) *Proc. Natl. Acad. Sci. U.S.A. 70*, 1790−3.
2. Levine, N. D. (1988) *J. Protozool. 35*, 518−20.
3. Boothroyd, J. C., Black, M., Bonnefoy, S., Hehl, A., Knoll, L. J., Manger, I. D., Ortega-Barria, E., and Tomavo, S. (1997) *Philos. Trans. R. Soc. Lond., Ser. B 352*, 1347−54.
4. Hill, D., and Dubey, J. P. (2002) *Clin. Microbiol. Infect. 8*, 634−40.
5. Tomavo, S. (2001) *Int. J. Parasitol. 31*, 1023−31.
6. Jones, J. L., Lopez, A., Wilson, M., Schulkin, J., and Gibbs, R. (2001) *Obstet. Gynecol. Surv. 56*, 296−305.
7. Mariuz, P. R., and Luft, B. J. (1992) in *AIDS Clinical Review 1992* (Volberding, D., and Jacobsen, M. A., Eds.) Chapter 5 (Toxoplasmic Encephalitis) pp 105−130 Marcel Dekker, New York.
8. Luft, B. J., and Remington, J. S. (1992) *Clin. Infect. Dis. 15*, 211−22.
9. Vander Jagt, D. L., Hunsaker, L. A., and Heidrich, J. E. (1981) *Mol. Biochem. Parasitol. 4*, 255−64.
10. Royer, R. E., Deck, L. M., Campos, N. M., Hunsaker, L. A., and Vander Jagt, D. L. (1986) *J. Med. Chem. 29*, 1799−801.
11. Dando, C., Schroeder, E. R., Hunsaker, L. A., Deck, L. M., Royer, R. E., Zhou, X., Parmley, S. F., and Vander Jagt, D. L. (2001) *Mol. Biochem. Parasitol. 118*, 23−32.
12. Yang, S., and Parmley, S. F. (1997) *Gene 184*, 1−12.
13. Stinson, R. A., and Gutfreund, H. (1971) *Biochem. J. 121*, 235−40.
14. Parker, D. M., Jeckel, D., and Holbrook, J. J. (1982) *Biochem. J. 201*, 465−71.
15. Gulotta, M., Deng, H., Dyer, R. B., and Callender, R. H. (2002) *Biochemistry 41*, 3353−63.
16. Gomez, M. S., Piper, R. C., Hunsaker, L. A., Royer, R. E., Deck, L. M., Makler, M. T., and Vander Jagt, D. L. (1997) *Mol. Biochem. Parasitol. 90*, 235−46.
17. Makler, M. T., and Hinrichs, D. J. (1993) *Am. J. Trop. Med. Hyg. 48*, 205−10.
18. Zhu, G., and Keithly, J. S. (2002) *J. Eukaryot. Microbiol. 49*, 255−61.
19. Wilks, H. M., Hart, K. W., Feeney, R., Dunn, C. R., Muirhead, H., Chia, W. N., Barstow, D. A., Atkinson, T., Clarke, A. R., and Holbrook, J. J. (1988) *Science 242*, 1541−4.
20. Otwinowski, Z., and Minor, W. (1997) *Methods Enzymol. 276*, 307−26.
21. Gehlhaar, D. K., and Fogel, D. B. (1999) *Acta Crystallogr., Sect. D 55*, 484−91.

22. Dunn, C. R., Banfield, M. J., Barker, J. J., Higham, C. W., Moreton, K. M., Turgut-Balik, D., Brady, R. L., and Holbrook, J. J. (1996) *Nat. Struct. Biol. 3*, 912−5.
23. Brünger, A. T., Adams, P. D., Clore, G. M., DeLano, W. L., Gros, P., Grosse-Kunstleve, R. W., Jiang, J. S., Kuszewski, J., Nilges, M., Pannu, N. S., Read, R. J., Rice, L. M., Simonson, T., and Warren, G. L. (1998) *Acta Crystallogr., Sect. D 54 (Pt 5)*, 905−21.
24. Jones, T. A., Zou, J.-Y., Cowan, S. W., and Kjeldgaard, M. (1991) *Acta Crystallogr., Sect. A 47*, 110−9.
25. Collaborative Computational Project, Number 4 (1994) *Acta Crystallogr., Sect. D 50*, 760−3.
26. Poole, L. B., and Ellis, H. R. (1996) *Biochemistry 35*, 56−64.
27. Laskowski, R. A., MacArthur, M. W., Moss, D. S., and Thornton, J. M. (1993) *J. Appl. Crystallogr. 26*, 283−91.
28. Chapman, A. D., Cortes, A., Dafforn, T. R., Clarke, A. R., and Brady, R. L. (1999) *J. Mol. Biol. 285*, 703−12.
29. Read, J. A., Winter, V. J., Eszes, C. M., Sessions, R. B., and Brady, R. L. (2001) *Proteins 43*, 175−85.
30. Hewitt, C. O., Eszes, C. M., Sessions, R. B., Moreton, K. M., Dafforn, T. R., Takei, J., Dempsey, C. E., Clarke, A. R., and Holbrook, J. J. (1999) *Protein Eng. 12*, 491−6.
31. Hewitt, C. O., Sessions, R. B., Dafforn, T. R., and Holbrook, J. J. (1997) *Protein Eng. 10*, 39−44.
32. Deleted in proof.
33. Eszes, C. M., Sessions, R. B., Clarke, A. R., Moreton, K. M., and Holbrook, J. J. (1996) *FEBS Lett. 399*, 193−7.
34. Pierce, A. C., Sandretto, K. L., and Bemis, G. W. (2002) *Proteins 49*, 567−76.
35. Engh, R. A., Brandstetter, H., Sucher, G., Eichinger, A., Baumann, U., Bode, W., Huber, R., Poll, T., Rudolph, R., and von der Saal, W. (1996) *Structure 4*, 1353−62.
36. Reddy, S. G., Scapin, G., and Blanchard, J. S. (1996) *Biochemistry 35*, 13294−302.
37. Kraulis, P. J. (1991) *J. Appl. Crystallogr. 24*, 946−50.
38. Merritt, E. A., and Bacon, D. J. (1997) *Methods Enzymol. 277*, 505−24.
39. Nicholls, A., Sharp, K. A., and Honig, B. (1991) *Proteins: Struct., Funct., Genet. 11*, 281−296.
40. Esnouf, R. M. (1997) *J. Mol. Graphics 15*, 113−138.

BI035108G